Molecular Physics, Vol. 105, Nos. 19–22, 10 October–20 November 2007, 2515–2525

Direct location of the minimum point on intersection seams of potential energy surfaces with equation-of-motion coupled-cluster methods

EVGENY EPIFANOVSKY and ANNA I. KRYLOV*
Department of Chemistry, University of Southern California, USA

(*Received 11 May 2007; in final form 29 June 2007*)

An implementation of the projected gradient method for locating the minimum energy crossing point between electronic states of different symmetry/multiplicity within the equation-of-motion coupled-cluster family of methods is reported. The method is applied to characterize the intersections between electronic states in N_3^+, NO_2, and *para*-benzyne using the excitation energies, ionization potential, and spin-flip variants of the equation-of-motion coupled-cluster methods. The performance of the algorithm is discussed and recommendations for improving the convergence in problematic situations are given.

Keywords: MECP; Conical intersections; Equation-of-motion; Coupled-cluster; Analytic gradients

1. Introduction

The dynamics of chemical reactions is often interpreted in terms of nuclear motions on a single potential energy surface (PES), which is based on the (non-relativistic) Born–Oppenheimer (BO), or adiabatic, approximation [1]. The BO approximation separates slow and fast degrees of freedom: the nuclei move in the mean field created by the electrons, which adjust their positions instantaneously. This is valid for many chemical reactions, however there is a plethora of processes for which the single-surface approximation breaks down [2]. Examples of such nonadiabatic processes, which involve transitions between different electronic states, include organic photochemistry [3] with a significant share of biologically important chemical reactions [4], as well as spin-forbidden processes [5].

Consider, for instance, the isomerization of retinal, an important step in the chemistry of vision [6]. A prototype reaction [7], the *cis–trans* photoisomerization of substituted ethylene, is sketched in figure 1. Upon electronic excitation, the system slides downhill towards the minimum on the excited state PES, which corresponds to a local maximum on the lower PES. At that point, the two surfaces approach each other, and the probability of a transition back to the ground state increases. Once on the ground state PES, the system relaxes to either the *cis*-or *trans*-product.

A set of points of confluence of two adiabatic PESs forming a continuous hyperline is called an intersection seam [8]. A nonadiabatic transition from one electronic state to another is more likely to happen near the crossing and is enabled by electronic couplings between the states. The nature of the coupling can be different: electronic states of the same multiplicity and symmetry can be coupled through the derivative coupling, while spin–orbit interaction facilitates the transition between states of different multiplicities. While the nonadiabatic transition can occur at any nuclear configuration, its probability is higher if the energy gap between the states is small.

A full description of a nonadiabatic process requires a calculation of nuclear dynamics that brings the system from the Franck–Condon region towards the point where the two states are nearly degenerate, and the probability of the nonadiabatic transition is larger (see, for example, [9, 10] and references therein). To describe the transition, both electronic and nuclear degrees of freedom should be considered.

Alternatively, one can gain considerable mechanistic insight and even quantitative information about the

*Corresponding author. Email: krylov@usc.edu

Molecular Physics
ISSN 0026–8976 print/ISSN 1362–3028 online © 2007 Taylor & Francis
http://www.tandf.co.uk/journals
DOI: 10.1080/00268970701549397

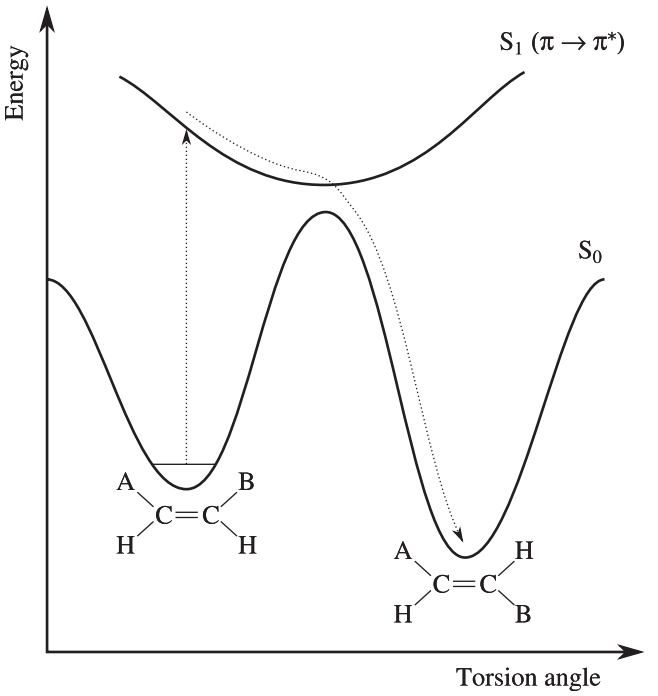

Figure 1. The potential energy surface slices for the ground and the first excited states of a substituted ethylene. There is an energy barrier that prevents the molecule from rotating freely around the double bond. The top of the barrier on the ground state PES corresponds to the minimum on the excited state PES.

probability of nonadiabatic transitions from the geometry and energy of the minimum energy point on the intersection seam (minimum energy crossing point, MECP, MSX) [11–19]. The MECP can be thought of as a characteristic point of the process, just like the transition state in a thermal chemical reaction. The energy of the MECP can help assess the possibility of the process, and with the use of the nonadiabatic transition state theory [20], the rate of the nonadiabatic process can be estimated. The geometry of MECP suggests which modes are most efficient in facilitating the transition [21].

Several methods of finding the MECP have been proposed over the past years [11–13, 15–19]. The crossing optimization procedure is very similar to that of finding the minimum on a PES, with the difference that constraints must be enforced to ensure the degeneracy of the states of interest. The algorithm of locating the MECP on a conical intersection seam is the same as for crossings of different symmetry or spin potential surfaces, only the constraints (and the dimensionality of the seam) are different.

Many methods employ the Lagrange multiplier technique to constrain the optimization. Some approaches require the calculation of a nonadiabatic coupling vector as well, which is rather demanding and have been implemented only for a handful of wavefunctions. For example, Ragazos *et al.* [12] and Manaa *et al.* [15] introduced analytical formalisms for the calculation of the nonadiabatic coupling vector at the multi-reference self-consistent field (MCSCF) and the multi-reference configuration interaction (MRCI) levels of theory and used it for seam minimization. Levine *et al.* [19] avoid the laborious evaluation of the coupling vector by using a tuning parameter. This implementation works with the time-dependent density functional theory (TD-DFT) for excited states.

This work reports an implementation of the projected gradient method [16] within the equation-of-motion coupled-cluster (EOM-CC) family of methods. The algorithm does not require the use of the Lagrange multiplier method and enables the constraints in the minimization procedure by projecting the energy gradient. The method was implemented within the Q-Chem quantum chemistry package [22].

The structure of the paper is as follows. The next section summarizes the theory of conical intersections and outlines the algorithm. Then EOM-CC methods are briefly reviewed. Section 4 presents several test cases and demonstrates the performance of the algorithm.

2. Theory

2.1. *Adiabatic approximation*

The full non-relativistic Hamiltonian of a molecular system $\mathbf{H}$ depends explicitly on both nuclear and electronic coordinates, $\mathbf{R}$ and $\mathbf{r}$, respectively:

$$\begin{aligned}\mathbf{H}(\mathbf{r},\mathbf{R}) &= \mathbf{T}_{\mathrm{n}}(\mathbf{R}) + \mathbf{T}_{\mathrm{e}}(\mathbf{r}) + \mathbf{V}_{\mathrm{ee}}(\mathbf{r}) + \mathbf{V}_{\mathrm{ne}}(\mathbf{r},\mathbf{R}) + \mathbf{V}_{nn}(\mathbf{R}) \\ &= \mathbf{T}_{\mathrm{n}}(\mathbf{R}) + \mathbf{H}_{\mathrm{e}}(\mathbf{r};\mathbf{R}),\end{aligned} \tag{1}$$

where $\mathbf{T}_{\mathrm{e}}$ and $\mathbf{T}_{\mathrm{n}}$ are electronic and nuclear kinetic energy operators, respectively, and $\mathbf{V}_{\mathrm{ee}}$, $\mathbf{V}_{\mathrm{ne}}$ and $\mathbf{V}_{\mathrm{nn}}$ are potential energy operators for electron–electron, nuclei–electron and nuclei–nuclei interactions. The electronic Hamiltonian $\mathbf{H}_{\mathrm{e}}(\mathbf{r};\ \mathbf{R})$ is defined as the full Hamiltonian minus the nuclear kinetic energy operator and thus depends explicitly on the electronic coordinates and only parametrically on the nuclear coordinates.

Eigenfunctions of the full Hamiltonian satisfy the Schrödinger equation:

$$\mathbf{H}(\mathbf{r},\mathbf{R})\Psi_i(\mathbf{r},\mathbf{R}) = \epsilon_i \Psi_i(\mathbf{r},\mathbf{R}). \tag{2}$$

The solutions of the so-called electronic Schrödinger equation are defined as follows:

$$\mathbf{H}_e(\mathbf{r},\mathbf{R})\phi_i(\mathbf{r};\mathbf{R}) = E_i\phi_i(\mathbf{r};\mathbf{R}), \tag{3}$$

and may be used as a basis to represent the full wavefunction $\Psi(\mathbf{r}, \mathbf{R})$:

$$\Psi(\mathbf{r},\mathbf{R}) = \sum_j \phi_j(\mathbf{r};\mathbf{R})\chi_j(\mathbf{R}), \tag{4}$$

where $\chi_j(\mathbf{R})$ are expansion coefficients called nuclear wave functions.

Substituting representation (4) into the full Schrödinger equation (2) and multiplying by ϕ_k from the left, we arrive at:

$$\sum_{k'} \langle\phi_k|\mathbf{H}_e + \mathbf{T}_n|\phi_{k'}\rangle_r \chi_{k'} = \epsilon \sum_{k''} \langle\phi_k|\phi_{k''}\rangle_r \chi_{k''}, \tag{5}$$

where the subscript r denotes integration over the electronic coordinates. After expanding $\mathbf{T}_n$ and using (3):

$$(\epsilon - E_k - \mathbf{T}_n - \mathbf{T}''_{kk})\chi_k = \sum_{k'\neq k} (\mathbf{T}'_{kk'} + \mathbf{T}''_{kk'})\chi_{k'}, \tag{6}$$

where

$$\mathbf{T}_n = -\sum_A \frac{1}{2M_A}\frac{\partial^2}{\partial R_A^2}, \tag{7}$$

$$\mathbf{T}'_{ij} = -\sum_A \frac{1}{M_A}\left\langle\phi_i\left|\frac{\partial}{\partial R_A}\right|\phi_j\right\rangle_r \frac{\partial}{\partial R_A}, \tag{8}$$

$$\mathbf{T}''_{ij} = -\sum_A \frac{1}{2M_A}\left\langle\phi_i\left|\frac{\partial^2}{\partial R_A^2}\right|\phi_j\right\rangle_r. \tag{9}$$

A solution to the coupled set of equations (6) yields $\chi_j(\mathbf{R})$, and therefore the solution to the full problem (2). If the off-diagonal terms on the right-hand side of (6) vanish, the overall wavefunction becomes just a single product of the electronic and nuclear parts, and the nuclear motions on different potential surfaces become uncoupled. This is the essence of the Born–Oppenheimer approximation: complete adiabatic separation of the nuclear and electronic motions (see, for example, [1]).

The approximation therefore requires that the coupling terms in (6) are small and can be neglected. Thus, it is important to understand when they may become significant. Using perturbation theory, one can rewrite the electronic part of the nonadiabatic coupling terms in (8) as

$$\left\langle\phi_i\left|\frac{\partial}{\partial\mathbf{R}}\right|\phi_j\right\rangle = \frac{\langle\phi_i|(\partial\mathbf{H}_e/\partial\mathbf{R})|\phi_j\rangle}{E_j - E_i}, \tag{10}$$

which suggests that the coupling between two electronic states becomes large when they are nearly degenerate. In such situations, the adiabatic approximation breaks down, and transitions between different electronic states become possible.

2.2. *Crossing location and minimization*

Although the set of equations (6) is infinite, the energy denominator in (10) suggests that the coupling between only two electronic states needs to be taken into account in the regions of proximity of their PESs, and the couplings with other states can be neglected.

The description of conical intersections and the algorithms for locating MECPs are based on a first-order perturbative treatment of the electronic Schrödinger equation in the vicinity of the intersection [8, 23]. Recently, second-order treatment that accounts for the curvature of the seam, in addition to the first-order linear terms, has been reported [24].

At the intersection point $\mathbf{R}$, the electronic Hamiltonian has the following matrix form in the so-called 'crude adiabatic basis' $\{\phi_i(\mathbf{r} : \mathbf{R}_0)\}$, eigenstates of the electronic Hamiltonian at a nearby point $\mathbf{R}_0$:

$$\mathbf{H}_e(\mathbf{R}) = \begin{pmatrix} H_{11} & H_{12} \\ H_{12} & H_{22} \end{pmatrix}, \tag{11}$$

where $H_{ij}(\mathbf{R}) = \langle\phi_i(\mathbf{r};\mathbf{R}_0)|\mathbf{H}_e(\mathbf{R})|\phi_j(\mathbf{r};\mathbf{R}_0)\rangle_r$.

After finding the eigenvalues of the Hamiltonian (11), one can readily write the conditions on the matrix elements that ensure that the states are degenerate:

$$\begin{cases} H_{11} - H_{22} = 0, \\ H_{12} = 0. \end{cases} \tag{12}$$

The above result is the essence of the Neumann–Wigner theorem, or the noncrossing rule [25], which states that two conditions have to be imposed on the Hamiltonian in order for the states to be degenerate and, therefore, limits the dimensionality of the intersection seam to $N-2$, where N is the number of internal degrees of freedom. If the coupling term is zero due to the symmetry restrictions (e.g., between the states of different spatial symmetry or different multiplicity), the dimensionality of the seam is $N-1$.

By applying degenerate perturbation theory (see, for example, [23]) to the eigenproblem with Hamiltonian (11), conditions (12) become

$$\begin{cases} \dfrac{\partial}{\partial \mathbf{R}}[E_1(\mathbf{R}) - E_2(\mathbf{R})]\Big|_{\mathbf{R}=\mathbf{R}_0} \delta\mathbf{R} = 0, \\ \left\langle \phi_1(\mathbf{r};\mathbf{R}) \left| \dfrac{\partial}{\partial \mathbf{R}} \right| \phi_2(\mathbf{r};\mathbf{R}) \right\rangle_r \Big|_{\mathbf{R}=\mathbf{R}_0} \delta\mathbf{R} = 0. \end{cases} \tag{13}$$

By defining the gradient difference vector,

$$\mathbf{g}(\mathbf{R}_0) = \frac{\partial}{\partial \mathbf{R}} E_1(\mathbf{R})|_{\mathbf{R}=\mathbf{R}_0} - \frac{\partial}{\partial \mathbf{R}} E_2(\mathbf{R})|_{\mathbf{R}=\mathbf{R}_0}, \tag{14}$$

and the derivative coupling vector,

$$\mathbf{h}(\mathbf{R}_0) = \left\langle \phi_1(\mathbf{r};\mathbf{R}) \left| \frac{\partial}{\partial \mathbf{R}} \right| \phi_2(\mathbf{r},\mathbf{R}) \right\rangle_r \Big|_{\mathbf{R}=\mathbf{R}_0}, \tag{15}$$

we arrive at

$$\begin{cases} \mathbf{g}(\mathbf{R}_0) \cdot \delta\mathbf{R} = 0, \\ \mathbf{h}(\mathbf{R}_0) \cdot \delta\mathbf{R} = 0. \end{cases} \tag{16}$$

Non-zero **g** and **h** vectors define a so-called **g**–**h**, or branching, plane [26, 27]. The degeneracy of the states is preserved in the subspace complement to the **g**–**h** plane and is lifted only along the plane. Thus, MECP can be found by following the gradient on one of the PES under constraint (16).

In this work, we implemented a reduced version of the projected gradient method [16] for locating the minimum energy point on an intersection. The method requires two vectors, the gradient difference **g** as defined in (14), the derivative coupling **h** as in (15), and the projection of the gradient on the higher PES onto the subspace orthogonal to the branching plane:

$$\mathbf{G}_2 = \mathbf{P}\frac{\partial}{\partial \mathbf{R}} E_2, \tag{17}$$

where **P** is the projector that performs the required operation. The gradient difference vector is multiplied by the energy difference in order to yield zero on the seam:

$$\mathbf{G}_1 = \frac{E_2 - E_1}{(|\mathbf{g}|^2)^{1/2}}\mathbf{g}. \tag{18}$$

The total gradient used in the optimization procedure is defined as

$$\mathbf{G} = \mathbf{G}_1 + \mathbf{G}_2. \tag{19}$$

Following $\mathbf{G}_1$, one arrives at the seam, while $\mathbf{G}_2$ is a gradient along the seam towards MECP.

The advantage of this technique is that it can be readily used with any existing optimization algorithm. The disadvantage is that it requires both gradients and nonadiabatic couplings.

Analytical calculations of the **h** vector have been implemented for the MCSCF and MRCI methods [12, 15]. For EOM-CC, however, only the mathematical procedure has been developed [28], and no implementation has been reported so far. In this work we consider the situations when the nonadiabatic derivative coupling vector is zero by symmetry, e.g. the spatial parts of the wavefunctions of the states carry different irreducible representations or the states are of different multiplicities. In this case, only analytic gradients are required [29].

2.3. *Equation-of-motion coupled-cluster method*

The EOM-CC approach [30–36] allows one to describe multi-configurational wavefunctions within a single-reference formalism. In this formalism, a similarity transformed Hamiltonian is introduced:

$$\bar{\mathbf{H}} = e^{-\mathbf{T}}\mathbf{H}e^{\mathbf{T}}, \tag{20}$$

where **T** is a general excitation operator. Regardless of the choice of **T**, the new Hamiltonian $\bar{\mathbf{H}}$ has the same spectrum as the original Hamiltonian **H**. An appropriate choice of **T**, however, ensures faster convergence w.r.t. many-electron basis set.

Target EOM states are obtained by diagonalizing $\bar{\mathbf{H}}$ in a basis of excited Slater determinants with respect to the reference $|\phi_0\rangle$ i.e. the following eigen-problem is solved:

$$\bar{\mathbf{H}}|\phi_0\rangle = E_i\mathbf{R}|\phi_0\rangle, \tag{21}$$

where **R** is another general excitation operator.

The approach is conceptually similar to configuration interaction (CI). In the limit of untruncated excitation operators, the EOM-CC wavefunctions are identical to those of full CI. However, truncated versions of EOM have advantages that make them superior to the corresponding CI methods, because EOM wavefunctions are size-extensive and correlation effects are 'wrapped-in' through the similarity transformation.

There are several versions of the EOM method that differ by the way the general excitation operator **R** produces many-electron basis functions from the reference state. The excitation energy (EOM-EE-CC) model [34] preserves the number of electrons and

forms the excitations by promoting one or more electrons from the occupied to the virtual orbitals. In the ionization potential (EOM-IP-CC) version [37–39], one electron is eliminated from the reference configuration to form the single excitations, and further excitations are produced thereon by electron promotion. The electron attachment (EOM-EA-CC) method is similar to EOM-IP-CC, only the single excitations are formed by adding an electron instead of removing one. Finally, in the spin-flip (EOM-SF-CC) model [36, 40, 41] the excited configuration set is formed from a high-spin reference and the excitation operators **R** flip the spin of an electron.

As a multi-state approach, EOM is very attractive for treating degenerate and nearly degenerate states. However, complications arise for true conical intersections due to non-Hermitian nature of the similarity transformed Hamiltonian [42, 43]. It has been recently discovered that complex energy values appear around the crossing points for truncated EOM models, spoiling the topology of the intersection [42]. A numerical example demonstrating the problem and a solution have also been reported [43]. The problem only comes about when dealing with intersections of PESs of the same symmetry. Thus, the topology of the intersections between the EOM states of different spatial or spin symmetry is described correctly, and no special treatment is required.

3. Benchmarks and examples

3.1. *Computational details*

All calculations were performed with the Q-Chem [22] package. Various versions of the EOM-CC method were employed for excited states calculations. The 6-31G basis set [44] was used for N_3^+ and NO_2, and 6-31G* basis [45]—for the *para*-benzyne diradical. To validate the code, MECPs were located by generating dense numerical grids for N_3^+ and NO_2. Then the algorithm was tested by setting the calculations with different starting geometries and employing different tolerance criteria.

3.2. *Cyclic trinitrogen cation*

The cyclic trinitrogen cation is a closed-shell system with a manifold of low-lying near-degenerate excited states [46, 47].

The equilibrium ground state geometry of N_3^+ is an equilateral triangle (D_{3h}), whereas low-lying excited states undergo Jahn–Teller distortions to C_{2v}. The C_{2v} point group symmetry will be used to label the excited states.

Both HOMO and LUMO in the ground state orbital picture of the cation are doubly degenerate. Therefore, four near-degenerate electronic states are derived upon the excitations from the highest occupied lone pair orbitals to the lowest unoccupied π^* orbitals. Among those, the 2^1A_2 and 1^1B^1 adiabatic states have PESs that form two intersection seams. One of the seams lies along the nuclear space coordinate that preserves the D_{3h} point group symmetry (this is the Jahn–Teller seam), and the other one is found in the subspace where the molecule is distorted from the equilateral triangular geometry to C_{2v}. There are three symmetry-identical MECP of the C_{2v} type.

This interesting feature—four very closely located conical intersections—was characterized by Dillon and Yarkony [47] and makes the intersection to appear glancing rather than conical [46].

As in the recent study [46], we employed EOM-EE-CCSD to describe the excited states of N_3^+. As long as the molecule preserves the C_{2v} symmetry, the wavefunctions of the electronic states of interest belong to different irreps, A_2 and B_1, and therefore the derivative coupling matrix element vanishes. The intersection seam between the states is two-dimensional.

To validate the algorithm, the $2^1A_2/1^1B_1$ crossing seams were first scanned in order to find the minimum energy points. The locations of these points, as well as the points of triple degeneracy, are listed in table 1.

To assess the performance of the algorithm, we attempted various geometries as the starting points for the optimization procedure. Usually the algorithm locates the minimum energy points on the $2^1A_2/1^1B_1$ seams in less than 20 iterations (table 2). Just like the local minimum on a global PES found with an optimization algorithm depending on the starting point, the seam located with the projected gradient method depends on the choice of the initial molecular geometry.

Another interesting feature of the manifold of the electronic states in N_3^+ is additional accidental degeneracies. The 1^1A_2 and 2^1A_2 are degenerate at a point in the internal coordinate space which happens to correspond to the molecule having the D_{3h} point group symmetry. Since 2^1A_2 and 1^1B_1 are rigorously degenerate in D_{3h}, the point becomes a point of a triple $1^1A_2/2^1A_2/1^1B_1$ intersection. The 1^1B_1 and 2^1B_1 electronic states have a point of degeneracy as well, which is therefore the point of a triple $2^1A_2/1^1B_1/2^1B_1$ intersection.

The $1^1A_2/2^1A_2/1^1B_1$ and $2^1A_2/1^1B_1/2^1B_1$ triple intersections were located at D_{3h} geometries with the N–N distance $R(NN) = 1.6671$ Å and

Table 1. Geometries and total energies of the intersection seam minima and points of triple degeneracy in N_3^+ calculated by EOM-CCSD/6-31G. All bond lengths are given in angstroms, all angles are given in degrees, all energies are given in au.

R(NN)	α(NNN)	$E(1^1A_2)$	$E\ (2^1A_2)$	$E\ (1^1B_1)$	$E(2^1B_1)$
D_{3h} seam minimum					
1.4556	60.00	−162.836 070	−162.822 635	−162.822 635	−162.816 033
C_{2v} seam minimum					
1.4476	60.78	−162.837 652	−162.821 903	−162.821 903	−162.815 864
Points of triple degeneracy					
1.6671	60.00	−162.795 662	−162.795 661	−162.799 368	−162.795 663
1.6041	60.00	−162.812 016	−162.807 857	−162.807 860	−162.807 858

Table 2. Results of energy minimization of the $2^1A_2/1^1B_1$ intersection seam in N_3^+ calculated by EOM-CCSD/6-31G. All bond lengths are given in angstroms, all angles are given in degrees.

Starting geometry			Final geometry	
R(NN)	α(NNN)	Iterations	R(NN)	α(NNN)
Tolerance[a] $\Delta g = 3 \times 10^{-4}$ (Q-Chem default)				
1.2000	60.00	6	1.4553	60.00
1.4200	60.00	4	1.4555	60.00
1.4600	70.00	16	1.4556	59.99
1.5400	50.00	5	1.4557	60.00
1.6000	90.00	8	1.4475	60.79
Tolerance $\Delta g = 3 \times 10^{-5}$				
1.2000	60.00	7	1.4556	60.00
1.4200	60.00	5	1.4556	60.00
1.4600	70.00	16	1.4556	59.99
1.5400	50.00	6	1.4556	60.00
1.6000	90.00	9	1.4476	60.78
Tolerance $\Delta g = 1 \times 10^{-5}$				
1.2000	60.00	7	1.4556	60.00[b]
1.4200	60.00	5	1.4556	60.00
1.4600	70.00	17	1.4556	60.00
1.5400	50.00	6	1.4556	60.00
1.6000	90.00	9	1.4476	60.78[c]

[a]Tolerance on the maximum gradient component. The optimization procedure converges if this and one of the two criteria—energy change $\Delta E = 10^{-6}$ au and maximum displacement $\Delta q = 1.2 \times 10^{-3}$ Å—are satisfied.
[b]Nuclear repulsion energy $E_{nr} = 53.441\,794$ au, total energy $E_{tot} = -162.822\,635$ au.
[c]Nuclear repulsion energy $E_{nr} = 53.528\,406$ au, total energy $E_{tot} = -162.821\,900$ au.

R(NN) = 1.6041 Å, respectively. Scans of the PESs around the points of intersections are shown in figure 2.

Note that the triple intersections are found at the D_{3h} symmetry and in fact are crossings of PESs belonging to different irreducible representations, even though it is not immediately clear from the C_{2v} notation. Therefore, the problem with complex energy values [43] does not arise.

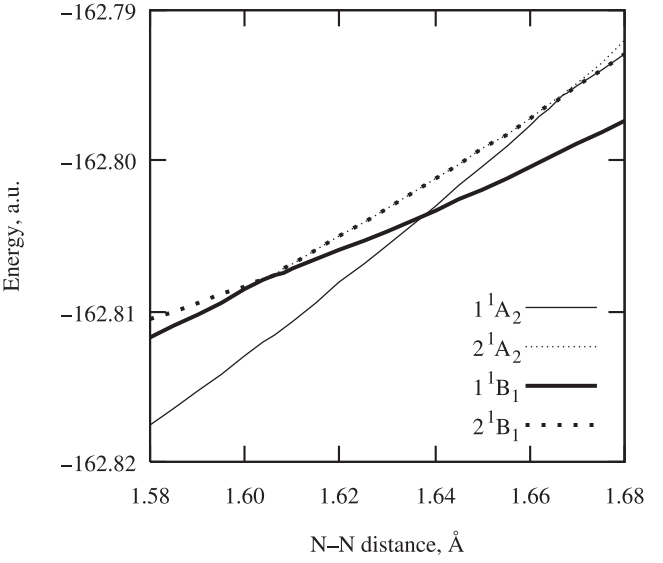

Figure 2. D_{3h}-constrained scans of adiabatic PESs of N_3^+ around the points of intersections calculated by EOM-CCSD/6-31G.

3.3. *Nitrogen dioxide*

The PESs of the ground and first excited states of the NO_2 molecule, X^2A_1 and A^2B_2, form an intersection [48]. Crossing points have been located for different N–O bond distances with the O–N–O angle between 107° and 108° [49].

When the molecule is constrained to the C_{2v} point group symmetry, the spacial parts of the wavefunctions of the states belong to different irreps, A_1 and B_2, and the derivative coupling matrix element between them vanishes.

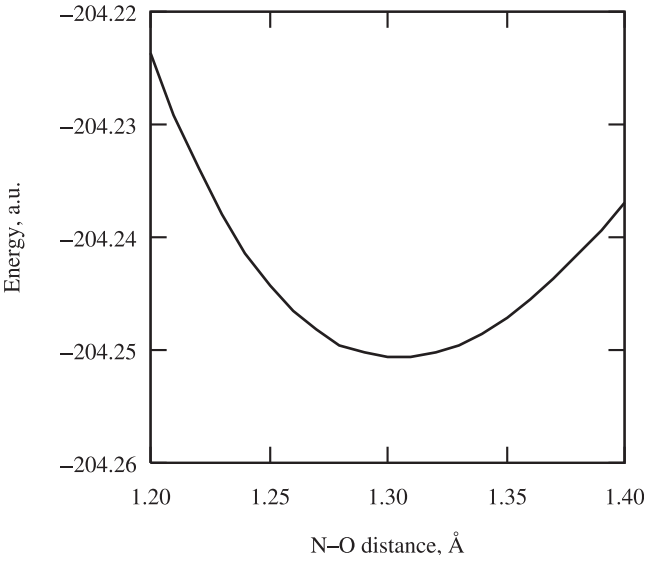

Figure 3. The seam of the X^2A_1/A^2B_2 intersection in nitrogen dioxide. At every N–O distance, the PESs of both states were scanned to find the O–N–O angle at which the states are degenerate.

Table 3. Points of the C_{2v} constrained seam of the X^2A_1/A^2B_2 intersection in nitrogen dioxide. All bond lengths are given in angstroms, all angles are given in degrees, all energies are given in au.

R(NO)	α(ONO)	$E(X^2A_1)$
1.2000	106.027	−204.223 693
1.2200	106.125	−204.233 934
1.2400	106.241	−204.241 419
1.2600	106.376	−204.246 503
1.2800	106.531	−204.249 495
1.3000	106.706	−204.250 673
1.3045	106.748	−204.250 713
1.3200	106.901	−204.250 279
1.3400	107.117	−204.248 528
1.3600	107.353	−204.245 608
1.3800	107.611	−204.241 686
1.4000	107.889	−204.236 910

Table 4. Results of C_{2v}-constrained energy minimization of the X^2A_1/A^2B_2 intersection seam in NO_2 calculated by EOM-IP-CCSD/6-31G. All bond lengths are given in angstroms, all angles are given in degrees.

Starting geometry			Final geometry	
R(NN)	α(ONO)	Iterations	R(NO)	α(ONO)
Tolerance[a] $\Delta g = 3 \times 10^{-4}$ (Q-Chem default)				
1.2000	100.00	13	1.3047	106.76
1.3000	90.00	14	1.3045	106.78
1.3000	120.00	15	1.3047	106.75
Tolerance $\Delta g = 3 \times 10^{-5}$				
1.2000	100.00	15	1.3046	106.74
1.3000	90.00	18	1.3046	106.75
1.3000	120.00	17	1.3046	106.75
Tolerance $\Delta g = 1 \times 10^{-5}$				
1.2000	100.00	17	1.3046	106.75[b]
1.3000	90.00	19	1.3046	106.75
1.3000	120.00	18	1.3046	106.75

[a]Tolerance on the maximum gradient component. The optimization procedure converges if this and one of the two criteria—energy change $\Delta E = 10^{-6}$ au and maximum displacement $\Delta q = 1.2 \times 10^{-3}$ Å—are satisfied.
[b]Nuclear repulsion energy $E_{nr} = 61.603\,681$ au, total energy $E_{tot} = -204.250\,712$ au.

If the symmetry is lowered further to the C_s point group symmetry, and the N–O bond lengths are allowed to vary independently, both the ground state and first excited state wavefunctions become of the A′ symmetry. The derivative coupling matrix element between the two states is no longer zero, and the intersection becomes truly conical.

The calculations were performed using the EOM-IP-CCSD method. The closed-shell CCSD wavefunction for NO_2^- was used as the reference for the EOM-IP calculations.

To locate and minimize the seam numerically, the two surfaces were first scanned. The N–O distance was varied from 1.20 to 1.40 Å, and at each point the O–N–O angle was varied from 90° to 130°, as shown in figure 3. These results are summarized in table 3. The minimum of the seam was located at $R(NO) = 1.3045$ Å, $\alpha(ONO) = 106.75°$.

Various starting geometries were used in order to test the performance of the algorithm. Table 4 contains the initial points attempted and the results obtained.

3.4. *Para-Benzyne diradical*

The *para*-benzyne diradical has the ^1A_g ground state and a low-lying $^3B_{1u}$ triplet excited state [50–55]. In both states, the equilibrium structure is of the D_{2h} point group symmetry.

The ground singlet state and the excited triplet state are derived from distributions of two electrons over the lower b_{1u} and the higher a_g frontier molecular orbitals. These states can be accurately described by the SF method [41] as spin-flipping excitations form the high-spin triplet reference state, as shown in figure 4.

The equilibrium geometries of the *para*-benzyne diradical were calculated at the EOM-SF-CCSD/6-31G* level. The geometries agree with the SF-DFT ones from [53], as shown in table 5.

Since the adiabatic singlet triplet gap is only about 0.03 eV, one could anticipate a low-energy $1A_g/^3B_{1u}$ intersection. The ground state equilibrium geometry found in [53] was used as the starting point for locating the minimum of the crossing seam. The convergence was achieved in about 50 iterations. The progress of the intersection optimization is shown in figure 6.

The MECP was located 0.65 eV above the ground state equilibrium energy as shown in the energy diagram in figure 7. The nuclear configuration at this point is significantly distorted compared to the ground state geometry. Note that although this distortion increases the splitting between the frontier MOs due to increased through-space interaction between the radical centres, it stabilizes the a_g orbital, due to the favourable through-bond interactions [57].

4. Discussion: Performance of the algorithm and details of implementation

Our implementation of the projected gradient algorithm employs the minimization technique used in Q-Chem: the Newton–Raphson method in conjunction with the eigenvalue following algorithm [58]. An approximate guess Hessian matrix used for the optimization is updated using the BFGS formula. We modified the EOM-CCSD/CCSD code [29] to allow simultaneous analytical calculation of the gradients for two states. The two components of the gradient (19) used in the minimization procedure are evaluated as given by (17) and (18).

We found that the convergence of the algorithm strongly depends on the relative absolute values of the two gradient components. If one of the components has a much greater absolute value than the other, after the step is taken, the smaller gradient changes its value significantly at the new point. Often, this leads to surges and oscillations of the energy during the minimization that spoils the convergence. For example, the optimization of the $^1A_g/^3B_{1u}$ intersection in the *para*-benzyne diradical fails if the $\mathbf{G}_1$ and $\mathbf{G}_2$ vectors are taken with the same weights, as in (19). We employed a modified version of the algorithm when the two components of the total gradient can be scaled with coefficients specified by the user. When the $\mathbf{G}_2$ vector is scaled such that its absolute value is approximately the same as that of the $\mathbf{G}_1$ vector, the procedure converges as shown in figure 6.

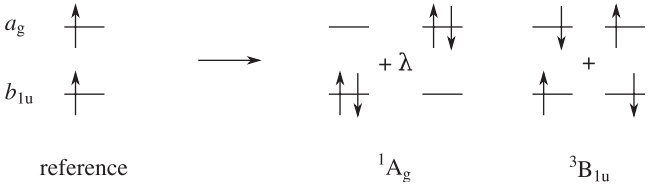

Figure 4. The singlet and the $M_s = 0$ triplet target states of the *para*-benzyne diradical derived from the high-spin triplet reference by spin-flip.

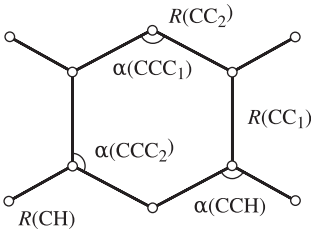

Figure 5. Geometrical parameters used to describe the *para*-benzyne diradical in table 5.

Table 5. Equilibrium geometries and the MECP of the ^1A_g and $^3B_{1u}$ electronic states calculated by EOM-SF-CCSD/6-31G*. Geometrical parameters are defined in figure 5. All bond lengths are given in angstroms, all angles are given in degrees.

Method	$R(CC_1)$	$R(CC_2)$	$R(CH)$	$\alpha(CCC_1)$	$\alpha(CCC_2)$	$\alpha(CCH)$
^1A_g ground state						
SF-DFT (50,50)/6-31G*[a]	1.419	1.358	1.077	124.8	117.6	123.6
CASSCF(8,8)/6-31G*[b]	1.411	1.383		124.0	118.0	
EOM-SF-CCSD/6-31G*[c]	1.424	1.374	1.087	124.4	117.8	123.0
$^3B_{1u}$ excited state						
SF-DFT (50,50)/6-31G*	1.398	1.370	1.079	126.8	116.6	122.3
CASSCF(8,8)/6-31G*	1.403	1.387		125.3	117.4	
EOM-SF-CCSD/6-31G*[d]	1.406	1.383	1.088	126.2	116.9	121.9
$^1A_g/^3B_{1u}$ intersection						
EOM-SF-CCSD/6-31G*[e]	1.388	1.366	1.101	137.4	111.3	124.0

[a]Reference [53]. [b]Reference [56]. [c]Nuclear repulsion energy $E_{nr} = 185.259\,520$ au., total energy $E_{tot} = -230.178\,701$ au. [d]Nuclear repulsion energy $E_{nr} = 185.220\,983$ au, total energy $E_{tot} = -230.171\,962$ au. [e]Nuclear repulsion energy $E_{nr} = 187.472\,024$ au, total energy $E_{tot} = -230.154\,762$ au.

In this context, the Lagrange multiplier algorithm (e.g. [14]) seems to be more robust, as it adjusts the coefficients automatically during the optimization procedure, thus insuring proper treatment of the problem. This, however, should not be considered a serious drawback of the projected gradient algorithm as with user-controlled coefficients comparable performance is achieved.

The scaling problem is related to the quality of the Hessian. In the straightforward implementation the approximate Hessian for the upper PES is used, which is not the Hessian of the function which is being optimized. The issue could be rectified by improving the Hessian update procedure. Alternatively, scaling coefficients can be used in order to improve convergence. By default, the components of the gradient are not scaled. However, the tests showed that scaling the $\mathbf{G}_2$ vector to one-tenth of its original absolute value significantly improves the convergence.

Yarkony [59] and Chachiyo and Rodriguez [17] addressed this problem by modifying the algorithms as follows. Rather than optimizing the energy difference, they minimize the average energy between the states, which demonstrated better performance.

5. Conclusions

We implemented a reduced variant of the projected gradient method [16] within the equation-of-motion coupled-cluster (EOM-CC) family of methods in the

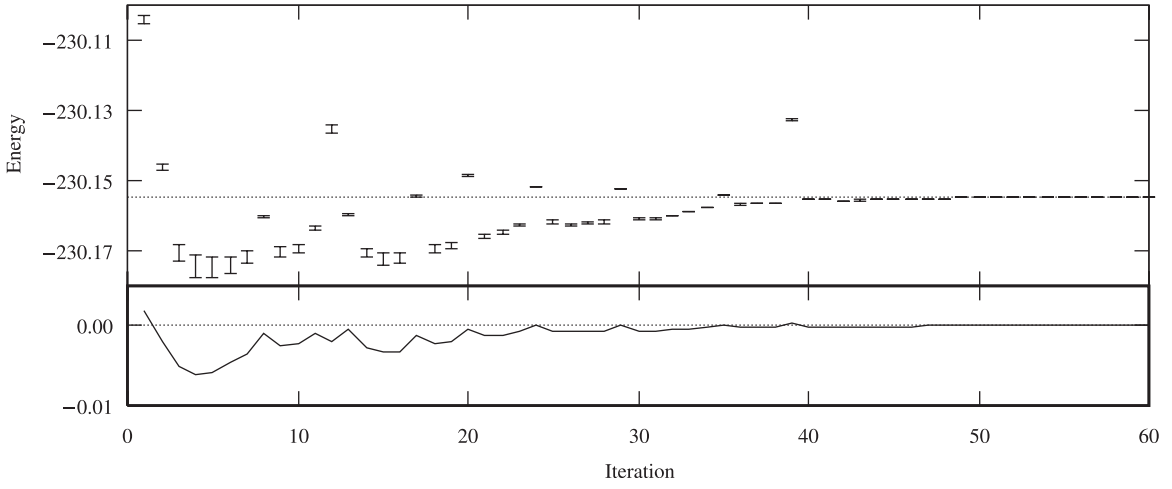

Figure 6. Convergence of the $^1Ag/^3B_{1u}$ intersection optimization in the *para*-benzyne diradical by EOM-SF-CCSD/6-31G*. In the upper part, the relative energies of both states are plotted for each iteration. The corresponding energy gaps are shown in the lower part. Convergence is achieved in about 50 iterations.

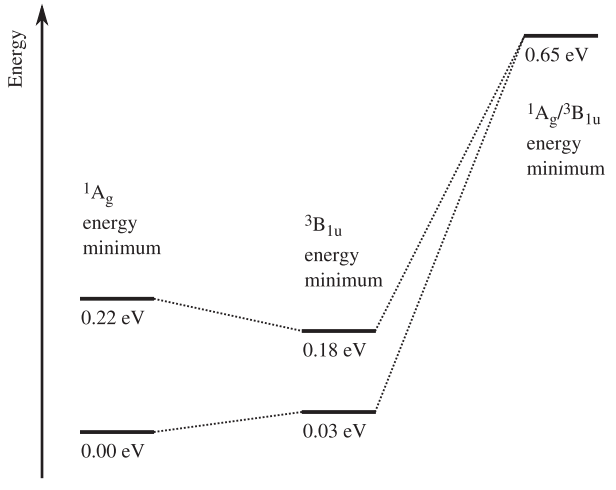

Figure 7. Relative energies of the ^1A_g and $^3B_{1u}$ states of *para*-benzyne diradical at their equilibrium structures and MECP. Both at the singlet and triplet equilibrium geometry, the singlet is below the triplet. The two states intersect 0.65 eV above the ground state minimum.

Q-Chem quantum chemistry package [22]. The algorithm employs analytic gradients [29] and assumes zero derivative couplings. Thus, it is applicable for minimizing the crossing seams between states of different symmetry and/or multiplicity. The method was applied to locate the MECPs between: (i) the excited states of N_3^+ described by EOM-EE-CCSD; (ii) the two lowest states of NO_2 described by EOM-IP-CCSD; and (iii) the singlet and triplet states of the *para*-benzyne diradical described by EOM-SF-CCSD.

The benchmarks demonstrated that the convergence depends on the quality of the initial guess, as well as local steepness/curvature of the seam, e.g. the convergence is poor when the magnitude of the two gradient components is very different. Scaling of the two components of the gradient was shown to improve the convergence.

Acknowledgements

This work was supported by the Department of Energy (DE-FG02-05ER15685). We also acknowledge the use of the resources of the Center for Computational Studies of Electronic Structure and Spectroscopy of Open-Shell and Electronically Excited Species (iopenshell.usc.edu) supported by the National Science Foundation through the CRIF:CRF CHE-0625419+0624602+0625237 grant.

References

[1] T. Helgaker, P. Jørgensen, and J. Olsen, *Molecular Electronic Structure Theory* (Wiley & Sons, New York, 2000).
[2] G. A. Worth and L. S. Cederbaum, Annu. Rev. Phys. Chem. **55,** 127 (2004).
[3] F. Bernardi, M. Olivucci, and M. A. Robb, Chem. Soc. Rev. **25,** 321 (1996).
[4] S. Olsen, A. Toniolo, C. Ko, L. Manohar, K. Lamothe, and T. J. Martínez, in *Computational Photochemistry*, edited by M. Olivucci (Elsevier, Amsterdam, 2007) (in the press).
[5] D. R. Yarkony, Int. Rev. Phys. Chem. **11,** 195 (1992).
[6] A. Warshel, Nature **260,** 769 (1974).
[7] M. Ben-Nun and T. J. Martínez, Chem. Phys. **259,** 237 (2000).
[8] D. R. Yarkony, Rev. Mod. Phys. **68,** 985 (1996).
[9] M. Ben-Nun, J. Quenneville, and T. J. Martínez, J. Phys. Chem. A **104,** 5161 (2000), and references therein.
[10] A. Toniolo, B. Levine, A. Thompson, J. Quenneville, M. Ben-Nun, J. Owens, S. Olsen, L. Manohar, and T. J. Martínez, in *Computational Methods in Organic Photochemistry*, edited by A. Kutateladze (Marcel-Dekker, New York, 2005).
[11] N. Koga and K. Morokuma, Chem. Phys. Lett. **119,** 371 (1985).
[12] I. N. Ragazos, M. A. Robb, F. Bernardi, and M. Olivucci, Chem. Phys. Lett. **197,** 217 (1992).
[13] D. R. Yarkony, J. Phys. Chem. **97,** 4407 (1993).
[14] D. R. Yarkony, J. Phys. Chem. A **105,** 6277 (2001).
[15] M. R. Manaa and D. R. Yarkony, J. Am. Chem. Soc. **116,** 11444 (1994).
[16] M. J. Bearpark, M. A. Robb, and H. B. Schlegel, Chem. Phys. Lett. **223,** 269 (1994).
[17] T. Chachiyo and J. H. Rodriguez, J. Chem. Phys. **123,** 094711 (2005).
[18] L. Serrano-Andrés, M. Merchán, and R. Lindh, J. Chem. Phys. **122,** 104107 (2005).
[19] B. G. Levine, C. Ko, J. Quenneville, and T. J. Martínez, Mol. Phys. **104,** 1039 (2006).
[20] Q. Cui, K. Morokuma, J. M. Bowman, and S. J. Klippenstein, J. Chem. Phys. **110,** 9469 (1999).
[21] S. Matsika, J. Phys. Chem. A **108,** 7584 (2004).
[22] Y. Shao, L. F. Molnar, Y. Jung, J. Kussmann, C. Ochsenfeld, S. Brown, A. T. B. Gilbert, L. V. Slipchenko, S. V. Levchenko, D. P. O'Neil, R. A. Distasio Jr, R. C. Lochan, T. Wang, G. J. O. Beran, N. A. Besley, J. M. Herbert, C. Y. Lin, T. Van Voorhis, S. H. Chien, A. Sodt, R. P. Steele, V. A. Rassolov, P. Maslen, P. P. Korambath, R. D. Adamson, B. Austin, J. Baker, E. F. C. Bird, H. Daschel, R. J. Doerksen, A. Drew, B. D. Dunietz, A. D. Dutoi, T. R. Furlani, S. R. Gwaltney, A. Heyden, S. Hirata, C.-P. Hsu, G. S. Kedziora, R. Z. Khalliulin, P. Klunziger, A. M. Lee, W. Z. Liang, I. Lotan, N. Nair, B. Peters, E. I. Proynov, P. A. Pieniazek, Y. M. Rhee, J. Ritchie, E. Rosta, C. D. Sherrill, A. C. Simmonett, J. E. Subotnik, H. L. Woodcock III, W. Zhang, A. T. Bell, A. K. Chakraborty, D. M. Chipman, F. J. Keil, A. Warshel, W. J. Herhe, H. F. Schaefer III, J. Kong, A. I. Krylov, P. M. W. Gill, and M. Head-Gordon, Phys. Chem. Chem. Phys. **8,** 3172 (2006).
[23] M. Dallos, H. Lischka, R. Shepard, D. R. Yarkony, and P. G. Szalay, J. Chem. Phys. **120,** 7330 (2004).
[24] F. Sicilia, L. Blancafort, M. J. Bearpark, and M. A. Robb, J. Phys. Chem. A **111,** 2182 (2007).
[25] J. von Neumann and E. Wigner, Z. Phys. **30,** 467 (1929).
[26] G. J. Atchity, S. S. Xantheas, and K. Ruedenberg, J. Chem. Phys. **95,** 1862 (1991).
[27] D. R. Yarkony, Acc. Chem. Res. **31,** 511 (1998).
[28] J. F. Stanton, J. Chem. Phys. **115,** 10382 (2001).
[29] S. V. Levchenko, T. Wang, and A. I. Krylov, J. Chem. Phys. **122,** 224106 (2005).
[30] D. J. Rowe, Rev. Mod. Phys. **40,** 153 (1968).
[31] K. Emrich, Nucl. Phys. A **351,** 379 (1981).
[32] H. Sekino and R. J. Bartlett, Int. J. Quant. Chem. Symp. **18,** 255 (1984).
[33] J. Geertsen, M. Rittby, and R. J. Bartlett, Chem. Phys. Lett. **164,** 57 (1989).
[34] J. F. Stanton and R. J. Bartlett, J. Chem. Phys. **98,** 7029 (1993).
[35] R. J. Bartlett and J. F. Stanton, Rev. Comp. Chem. **5,** 65 (1994).
[36] S. V. Levchenko and A. I. Krylov, J. Chem. Phys. **120,** 175 (2004).
[37] J. F. Stanton and J. Gauss, J. Chem. Phys. **101,** 8938 (1994).
[38] M. Nooijen and R. J. Bartlett, J. Chem. Phys. **102,** 3629 (1995).

[39] D. Sinha, D. Mukhopadhya, R. Chaudhuri, and D. Mukherjee, Chem. Phys. Lett. **154,** 544 (1989).
[40] A. I. Krylov, Chem. Phys. Lett. **338,** 375 (2001).
[41] A. I. Krylov, Acc. Chem. Res. **39,** 83 (2006).
[42] C. Hättig, Adv. Quant. Chem. **50,** 37 (2005).
[43] A. Köhn and A. Tajti, J. Chem. Phys. **127**, 044105 (2007).
[44] W. J. Hehre, R. Ditchfield, and J. A. Pople, J. Chem. Phys. **56,** 2257 (1972).
[45] P. C. Hariharan and J. A. Pople, Theor. Chim. Acta **28,** 213 (1973).
[46] V. A. Mozhayskiy, D. Babikov, and A. I. Krylov, J. Chem. Phys. **124,** 224309 (2006).
[47] J. J. Dillon and D. R. Yarkony, J. Chem. Phys. **126,** 124113 (2007).
[48] C. F. Jackels and E. R. Davidson, J. Chem. Phys. **64,** 2908 (1976).
[49] G. Hirsch, R. J. Buenker, and C. Petrongolo, Molec. Phys. **70,** 835 (1990).
[50] E. Kraka and D. Cremer, J. Am. Chem. Soc. **116,** 4929 (1994).
[51] T. D. Crawford, E. Kraka, J. F. Stanton, and D. Cremer, J. Chem. Phys. **114,** 10638 (2001).
[52] L. V. Slipchenko and A. I. Krylov, J. Chem. Phys. **117,** 4694 (2002).
[53] Y. Shao, M. Head-Gordon, and A. I. Krylov, J. Chem. Phys. **118,** 4807 (2003).
[54] H. H. Wenk, M. Winkler, and W. Sander, Angew. Chem. Int. Ed. Engl. **42,** 502 (2003).
[55] V. Vanovschi, A. I. Krylov, and P. G. Wenthold, Theor. Chim. Acta (2007) (in the press).
[56] A. E. Clark and E. R. Davidson, J. Am. Chem. Soc. **123,** 10691 (2001).
[57] K. K. Baldridge, T. R. Buttersby, R. V. Clark, and J. S. Siegel, J. Am. Chem. Soc. **119,** 7048 (1997).
[58] J. Baker, J. Comp. Chem. **7,** 385 (1986).
[59] D. R. Yarkony, Faraday Discuss. **127,** 325 (2004).